



An interactive study of catalyst and mechanism for electrochemical CO₂ reduction to formate on Pd surfaces

Tian-Wen Jiang^a, Xianxian Qin^a, Ke Ye^b, Wei-Yi Zhang^a, Hong Li^a, Wenhui Liu^d, Shengjuan Huo^d, Xia-Guang Zhang^{c,*}, Kun Jiang^{b,*}, Wen-Bin Cai^{a,*}

^a Shanghai Key Laboratory of Molecular Catalysis and Innovative Materials, Collaborative Innovation Center of Chemistry for Energy Materials, Department of Chemistry, Fudan University, Shanghai 200438, China

^b Interdisciplinary Science Research Centre, School of Mechanical Engineering, Shanghai Jiao Tong University, Shanghai 200240, China

^c Key Laboratory of Green Chemical Media and Reactions, Ministry of Education, Collaborative Innovation Center of Henan Province for Green Manufacturing of Fine Chemicals, College of Chemistry and Chemical Engineering, Henan Normal University, Xinxiang 453007, China

^d International Joint Laboratory of Catalytic Chemistry, Institute for Sustainable Energy, Department of Chemistry, College of Sciences, Shanghai University, Shanghai 200444, China



ARTICLE INFO

Keywords:
CO₂RR to formate
Interactive study
Pd-based catalyst
Reaction mechanism
ATR-SEIRAS

ABSTRACT

Electrochemical CO₂ reduction reaction to formate (CO₂RRTF) on Pd-based surfaces merits very low overpotentials, yet is challenged with identification of a high-performance catalyst and validation of the reaction pathway. In this work, an interactive study of catalyst and mechanism is presented to address the above bottleneck. On one hand, inspired by preliminary mechanistic understanding of HCOOH \leftrightarrow CO₂ interconversion at Pd surfaces, a Bi-modified Pd/C with the known high performance towards formic acid dehydrogenation (FAD) is elected as the prototype candidate catalyst for CO₂RRTF, exhibiting indeed significantly higher activity, selectivity, durability and extended working potentials. On the other hand, the CO₂ chemical hydrogenation mechanism is clarified with monodentate formate being the key intermediate for CO₂RRTF on Pd surfaces, by applying isotope labeled ATR-SEIRAS measurement and kinetic analysis in conjunction with DFT calculations. The research paradigm facilitates locating efficient catalysts and advancing mechanistic study for CO₂RRTF on Pd surfaces and beyond.

1. Introduction

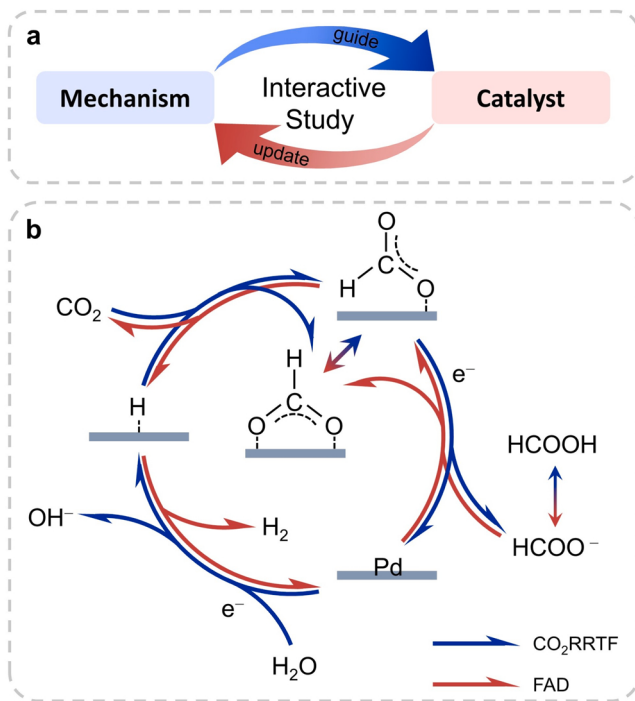
Electrochemical CO₂ reduction reaction (CO₂RR) to valuable chemicals and feedstocks driven by renewable power electricity is an alternative strategy to decrease the CO₂ content in the atmosphere and achieve carbon neutrality [1–3]. Among the reduction products of CO₂RR, formic acid (or its conjugated base formate) is one of the most noticeable chemicals with the highest net present values and economic benefits [4,5], and the liquid product can be fed into a direct formic acid fuel cell, or used as a hydrogen storage chemical or a precursor for other value-added chemicals [6–9]. Unlike high-overpotential metals such as Sn [10–12], Bi [13–15] and In [10,16,17] for CO₂RR to formic acid-formate (CO₂RRTF), Pd is unique and attractive in electro-catalyzing two-electron interconversion between formic acid-formate and CO₂ around the equilibrium potential of the CO₂/HCOOH-formate redox [18–23]. Nevertheless, the predominant interconversion is

accompanied with a gradual deactivation of the Pd catalyst due to surface CO accumulation, as confirmed spectroscopically [19–21,24,25]. Besides, the selective CO₂RRTF is often limited to a narrow potential range, beyond which gaseous CO tends to become the major product [26–33]. Therefore, locating higher performance Pd-based catalysts and advancing the mechanistic understanding towards CO₂RRTF are two major tasks in this field [34–40]. So far, these two aspects are mostly considered separately.

The interactive study of catalyst and mechanism is a new and effective paradigm as compared to traditional trial and error in developing catalysts and clarifying mechanisms for CO₂RR. In this paradigm (see Scheme 1a), on one hand, for a reaction of interest, a candidate catalyst is elected according to the analysis of existing knowledge and mechanism, and testified experimentally; on the other hand, based on new data on the examined catalyst, the existing mechanism is polished and renewed accordingly. At the equilibrium potential, the forward and

* Corresponding authors.

E-mail addresses: zhangxiuguang@htu.edu.cn (X.-G. Zhang), kunjiang@sjtu.edu.cn (K. Jiang), wbc@fudan.edu.cn (W.-B. Cai).



Scheme 1. (a) Illustration of the interactive study between mechanism and catalyst. (b) The reversed reaction pathways for FAD and CO₂RRTF.

backward reaction rates are equal and a catalyst promotes the bidirectional reactions at a same rate [41]. It can be hypothesized that for the above reversible CO₂/HCOOH redox system at potentials biased not far from the equilibrium potential, a Pd-based catalyst for one directional reaction could be also applied for the other. Also notably, at potentials of steady formic acid decomposition to H₂ (FAD) or CO₂RRTF, β -Pd hydride may form given a sufficient period of time [42–44]. The observed reversible interconversion suggests that a common intermediate in the forward and backward reactions exists, which is widely regarded as an adsorbed formate (HCOO^{*}) in the literature [45–50]. Along this line, a superb FAD Pd-based catalyst with weakened adsorption of H^{*} and *CO and strengthened adsorption of HCOO^{*} [51], is likely a promising candidate for CO₂RRTF, and vice versa.

A plausible FAD mechanism involves the electro-sorption of a formate ion followed by the dehydrogenation of adsorbed formate and the recombination of adsorbed H, as shown in the red pathway of Scheme 1b. For CO₂RRTF, the so-called proton coupled electron transfer (PCET) was reported with a bidentate HCOO_B^{*} as the intermediate [2, 45, 48, 52, 53]. Alternatively, a mechanism involving CO₂⁻ was also mentioned. The PCET and CO₂⁻ mechanisms may apply to high overpotential metals on which the H binding strength is very weak and the polarization overpotential is very high [54–57]. In contrast, on Pd surfaces only a very small potential bias is needed for a steady CO₂RRTF, arguing strongly against the involvement of CO₂⁻. Moreover, the strong affinity of H to Pd raises a great possibility of H adsorption [26, 43, 58, 59] followed by its combination with CO₂ to form the HCOO^{*}-intermediate via the so-called chemical hydrogenation (CH) mechanism [19, 38, 52, 60–67], largely following the reaction steps reverse to those for FAD, as shown in the blue pathway of Scheme 1b.

Indirect evidences in support of the CH mechanism on Pd-based catalysts have shown up recently. An increased surface H coverage on Pd achieved by introducing gaseous H₂ into a CO₂RR system promotes the production of formate [64, 68], consistent with the CH mechanism. The HCOO⁻ yield on PdH_{0.5}/C was reported to be proportional to the catalyst loading in D₂O solution while no HCOO⁻ production was detected on Pd/C in otherwise same conditions, consistent with the CH mechanism given that the PdH_{0.5}/C catalyst provides the H source for

CO₂RRTF [38]. In addition, a kinetic analysis suggests that α -PdH is active for CO₂RRTF [39]. Nevertheless, the clarification of the CH mechanism for CO₂RRTF yet needs direct molecular level evidences. Although HCOO^{*} is commonly suggested as the intermediate in the bidirectional reactions, it is not clear which conformational HCOO^{*} (bidentate or monodentate) is the immediate precursor in the CO₂RRTF conversion. HCOO_B^{*} is only detected spectrally at potentials above 0.2 V while HCOO_M^{*} has not been detected in formic acid oxidation (FAO) on Pd [69–72]. In the case of CO₂RRTF on Pd surfaces, no concrete spectral evidence in support of HCOO^{*} intermediate was provided [26, 73–76].

In this work, we present an interactive study of catalyst and mechanism for CO₂RRTF to address the above concerns. A Bi adatom-modified Pd/C (Pd-Bi_x/C) catalyst known to deliver a superb performance towards FAD, employed here as a prototype for the interactive study, is elected as the target catalyst for CO₂RRTF according to the existing mechanism analysis, and indeed yields higher selectivity, activity, durability as well as a wider potential window compared to a Bi-free Pd/C catalyst. Isotope labeled in-situ attenuated total reflection surface-enhanced infrared absorption spectroscopy (ATR-SEIRAS) in conjunction with density functional theory (DFT) calculations is applied to clarify the mechanism of the CO₂RRTF on Pd surfaces including the in-depth understanding of the enhanced CO₂RRTF on Pd-Bi_x/C. Notably, spectroscopic evidence of HCOO_M^{*} as formed in CO₂RRTF conversion is carefully presented, validating the CH mechanism.

2. Experimental section

2.1. Chemicals

Palladium chloride dehydrate (PdCl₂) was purchased from Aldrich. Carbon black (Vulcan XC-72) was purchased from Cabot Co. Sodium borohydride (NaBH₄), bismuth oxide (Bi₂O₃), trisodium citrate dihydrate (Na₃Cit·2 H₂O), nitric acid (HNO₃), ascorbic acid (C₆H₈O₆) and potassium bicarbonate (KHCO₃) were purchased from Sinopharm Chemical Reagent. Perchloric acid (HClO₄) were purchased from Aladdin. All the reagents were used as received. All solutions were prepared with ultrapure Milli-Q water with a resistivity of 18.2 MΩ cm.

2.2. Preparation of Pd/C and Pd-Bi_x/C

Pd/C and Pd-Bi_x/C (20 wt%, a typical loading for Pd/C in electrocatalytic characterization [26, 36, 38]) were synthesized according to the previously reported methods [51, 77]. Briefly, Pd/C was prepared by an aqueous reduction method as described below. 80 mg of carbon black, 450 mg of Na₃Cit·2 H₂O and 1.68 mL of 0.11 M Na₂PdCl₄ were added into 40 mL of Milli-Q water, and dispersed by sonication and stirring. Then 10 mL of 0.13 M NaBH₄ (containing 0.05 M Na₂CO₃) was added dropwise into the suspension, which was then kept under stirring overnight. At last, it was filtered and washed for several times, and dried at vacuum at 343 K overnight.

Pd-Bi_x/C catalysts were prepared by Bi(III) spontaneous adsorption and/or ascorbic acid reduction [75]. It should be pointed out that the amount of Bi-modification on 20 wt% Pd/C was limited up to a coverage of ca. 0.33 by direct spontaneous adsorption, so ascorbic acid was additionally introduced to prepare Pd-Bi_x/C with higher Bi coverages. 80 mg of Pd/C was dispersed into 40 mL of Milli-Q water by sonication and stirring. A certain amount of 20 mM Bi(NO₃)₃ solution and ascorbic acid were added into the suspension under stirring, see Table S1 for details. Then, it was filtered, washed and dried in the same procedure as described before.

2.3. Characterization of catalysts

The component of the Pd/C and Pd-Bi_x/C catalysts (see Table S2) were analyzed by inductively coupled plasma atomic emission

spectroscopy (ICP-AES) on a Hitachi P-4010 spectrometer. The morphology and size distributions of Pd and Pd-Bi_x/C nanoparticles were characterized by Field Emission Transmission Electron Microscope (Tecnai G2 F20 S-Twin). The crystalline phases of Pd/C and Pd-Bi_x/C were characterized by means of X-ray diffraction (XRD) on a D8 Advance and Davinci Design X-ray diffractometer with the Cu K α radiation scanning from 20° to 90°. X-ray photoelectron spectroscopy (XPS) was run on a Perkin Elmer PHI-5000 C ECSA system equipped with a hemispherical electron energy analyzer using monochromatic Mg K α radiation (1253.6 eV). The binding energies were calibrated with reference to the C 1 s peak at 284.6 eV.

2.4. Electrochemical CO₂RR measurement

The CO₂RR electrolysis was carried out at room temperature in an H-type cell as described in previous report [40]. The catalyst inks were prepared by ultrasonically dispersing 5 mg of catalysts in 800 μ L of water, 200 μ L of isopropanol, and 120 μ L of 5 wt% Nafion solution. Around 56.3 μ L of this ink was drop-coated onto the glassy carbon electrode (dia. 8 mm) with a Pd loading of 100 μ g cm⁻², and dried under an infrared lamp. The quantification of as-produced formate was done by an ion chromatography (Spectrap IC1820) with the mobile phase of an aqueous solution of KOH (5 mM, flowing at 0.6 mL min⁻¹). The gaseous CO and H₂ product were detected by on-line gas chromatography (Ramiin Instruments GC2060) equipped with a flame ionization detector (FID) coupled with a methanator and a thermal conductivity detector (TCD).

2.5. Electrochemical ATR-SEIRAS measurement

A Pd/C or Pd-Bi_{0.33}/C coated Au/Si was used as the working electrode with an SCE and a carbon rod being the reference and counter electrodes, respectively. The details of the ATR-SEIRAS setup were described previously [21,78]. Briefly, ATR-SEIRAS spectra were acquired at a resolution of 4 cm⁻¹ with unpolarized IR radiation at an incidence angle of ca. 70° by a Nicolet iS50 FTIR spectrometer with a built-in MCT detector. All the spectra are shown in the absorbance unit as $-\log(I/I_0)$, where I and I_0 represent the intensities of the reflected radiation of the sample and reference spectra, respectively.

2.6. Calculation detail

Vienna Ab Initio Simulation Package [79] (VASP 6.3.0 version) with the Perdew-Burke-Ernzerhof functional was used to perform all the density functional theory calculation. The Pd(111) (2 × 2) supercell, Bi/Pd(111) (4 × 2) supercell, and Bi/Pd(211) (2 × 2) supercell surfaces, with 15 Å vacuum layer were built, with Bi adatoms adsorbed on the fcc site of Pd(111) surface. The k-point of 6 × 6 × 1 and 3 × 6 × 1 were used for Pd(111) and Bi/Pd(111) surfaces, respectively. The wave energy cutoff was set at 450 eV, convergence criterion of electronic energy and forces were set at 10⁻⁶ and 0.02 eV, respectively. The water solution was simulated using the Poisson-Boltzmann implicitly solvent model at VASPsol software [80,81], the relative permittivity was set at 78.4. Vibrational frequencies of adsorbed intermediates were calculated by the finite difference method, and all metal atoms were fixed.

3. Results and discussion

3.1. Catalytic performances on targeted catalysts

As claimed in the Introduction Section, a promising Pd-based catalyst possesses a likelihood to be shared both for FAD and CO₂RR. The Bi-modified Pd/C catalyst which proved to be efficient for FAD to form H₂ and CO₂ by this group is expected to work well also for the CO₂RR to formate. Consequently, Pd-Bi_x/C catalysts (i.e., Bi adatoms modified Pd nanoparticles on carbon black) with various surface Bi coverages (θ_{Bi})

are thus prepared through the spontaneous adsorption of Bi(III) on Pd (or in the presence of ascorbic acid), where x represents the θ_{Bi} .

The θ_{Bi} is evaluated by cyclic voltammograms (CVs) within the hydrogen adsorption-desorption region as shown in Fig. 1a, corresponding to the reduced percentages of the peak area [51,82]. Compositional and structural characterizations are performed on Pd/C and Pd-Bi_x/C, as shown in Fig. 1 and Figs. S1–S4, the results conform to our previous report [51]. In short, Bi atoms exist essentially in the form of adatoms without disturbing the Pd lattice or constructing an individual crystalline phase, and partial electron transfer occurs from Bi adatoms to Pd surface atoms [40,83] (the binding energy of Pd⁰ 3d_{5/2} shifts from 335.5 eV for Pd/C to 335.8 eV for Pd-Bi_{0.33}/C, see Fig. 1b). Bi adatoms exist in the form of Bi(III) at ambient condition as shown in Fig. 1c, while during CO₂RR at negative potentials, Bi(III) can be reduced to metallic state given that the working potential is much more negative than the redox potential of Bi(III)/Bi(0). The metallic nanoparticles of Pd/C and Pd-Bi_{0.33}/C disperse homogeneously on the carbon support with statistical mean sizes located at ~3.4 nm and ~3.5 nm, respectively (see Figs. 1d and 1e). The electrochemical active surface area of Pd/C is ca. 87 m² g⁻¹ as estimated by CO stripping (Fig. S4). Note: Pd-Bi_{0.33}/C in this work where the subscript 0.33 stands for surface coverage corresponds to Pd@Bi_{0.11} in Ref 49 where the subscript 0.11 stands for the overall atomic ratio of Bi to Pd.

Given the as-synthesized Pd-Bi_{0.33}/C catalyst is liberally the one most effective for FAD in Pd-Bi_x/C and Pd/C, we examined it for electrocatalyzing CO₂RR as inspired by the existing mechanism analysis. Fig. 2a displays the linear sweep voltammograms (LSVs) of Pd/C and Pd-Bi_{0.33}/C in Ar- or CO₂-saturated 0.1 M KHCO₃ recorded at 50 mV s⁻¹. At potentials 0 ~ -0.5 V, the currents in the CO₂-saturated electrolyte are larger than that in the Ar-saturated one due to the efficient CO₂RR at this potential region. The situation inverts at potentials negative of -0.5 V, due to a suppressed hydrogen evolution reaction (HER) and an increased CO poisoning in the CO₂-saturated electrolyte. Bi adatom modification alleviates the CO poisoning during CO₂RR, as demonstrated by cyclic voltammetry in Ar- or CO₂-saturated 0.1 M KHCO₃. For clarity, only the negative scan voltammograms are presented in Fig. S5, showing that the reduction current on Pd-Bi_{0.33}/C decays to a less extent (ca. 10 %) than Pd/C with potential cycling.

Figs. 2b and 2c show the faradaic efficiencies (FEs) of CO₂RR products formate and CO and byproduct H₂ on Pd/C and Pd-Bi_{0.33}/C from -0.1 to -0.8 V, for comparison Fig. S6 also shows those on Pd-Bi_x/C with differing Bi coverages. All the catalysts exhibit a typical product transition from formate to CO as the potential moves negatively. Specifically, the potential dependent FE(formate) on different catalysts are replotted and compared in Fig. 2d while those for CO and H₂ are in Fig. S7. The FEs for formate and CO show opposite sigmoidal potential dependence, and the FE for H₂ shows a bell-shape dependence. Obviously, as compared to the pristine Pd/C, appropriate modification of Bi adatoms on Pd nanoparticles increases the FE(formate) at all tested potentials and broadens the potential window for formate production (also seen in Fig. S8) with an optimal Bi coverage of 0.33, which coincides with the optimal one that promotes FAD [51]. Specifically, Pd-Bi_{0.33}/C shows the highest FE(formate) of 97.7% at -0.2 V, and it maintains higher than 95% at potentials \geq -0.3 V, while it is only ca. 90% on Pd/C at -0.1 and -0.2 V and decays rapidly at more negative potentials. However, an excessive Bi-modification ($\theta_{Bi} > 0.5$) dramatically reduces the formate selectivity, along with a failure in the suppression of HER. It is worth noting that in the present work, the effective working potentials for the CO₂RR on Pd/C and Pd-Bi_{0.33}/C are similarly located at lower overpotentials (0 ~ -0.4 V), in stark contrast to those on Bi-based catalysts [13–15]. In other words, both Pd/C and Pd-Bi_{0.33}/C exhibit essentially catalytic behaviors of Pd-based catalysts rather than Bi-based ones.

To compare the CO₂RR activities on these catalysts, partial currents of formate in Pd mass activity (mA mg⁻¹ as the unit) are calculated and plotted versus potential, as shown in Fig. 2e. The catalysts show a

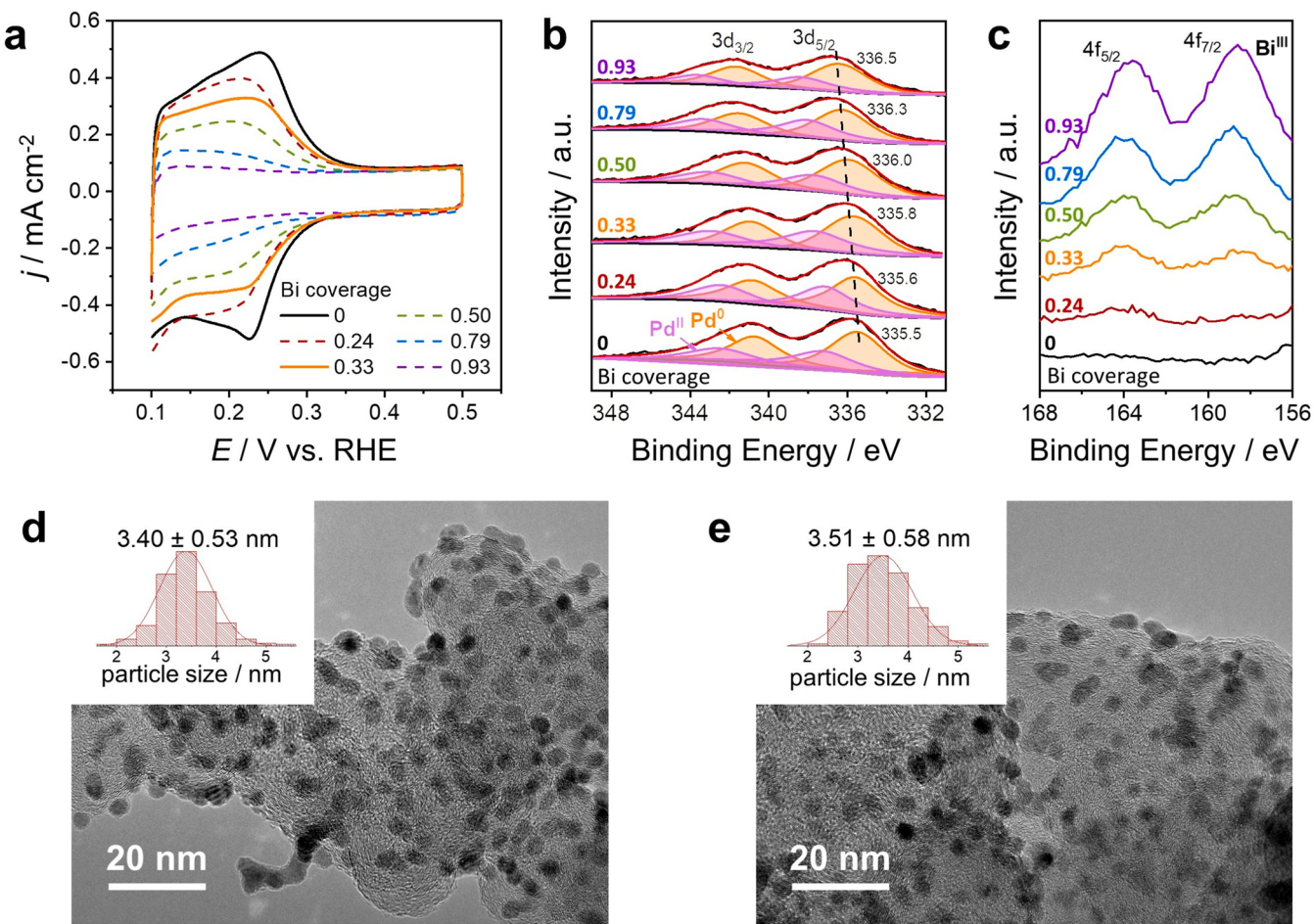


Fig. 1. (a) Cyclic voltammograms for Pd/C and Pd-Bi_x/C in 0.1 M HClO₄ between 0.1 and 0.5 V recorded at 10 mV s⁻¹. (b) Pd 3d and (c) Bi 4f core-level XPS spectra for Pd/C and Pd-Bi_x/C. (d, e) TEM images for Pd/C and Pd-Bi_{0.33}/C, along with the particle size distributions.

typical volcano shape in term of the partial currents as a function of the potential, the vertices of which are located at ca. -0.3 V. The highest partial current for formate production is attained at -0.3 V on Pd-Bi_{0.33}/C with a mass activity of 38.3 mA mg_{Pd}⁻¹, which is 1.7 times as much as that on Pd/C (i.e., 22.2 mA mg_{Pd}⁻¹) under otherwise same conditions. Table S3 compares the reported CO₂RRTF mass activities on Pd-based catalysts, showing a very high ranking for the Pd-Bi_{0.33}/C catalyst, although the measurement conditions in literature reports may differ to some extent. The Bi coverage dependent turnover frequencies based on global Pd sites (TOF_g) for CO₂RRTF at -0.3 V and FAD at 303 K (data obtained from Ref. 49) on Pd-Bi_x/C catalysts are plotted in Fig. 2f. The Bi-modified Pd/C catalysts show similar dependence on Bi coverage of CO₂RRTF and FAD catalytic activities, manifesting the targeted catalyst can be indeed shared for the two catalytic reactions as assumed in the Introduction Section.

To investigate the effect of Bi-modification on catalyst durability, chronoamperometry on Pd/C and Pd-Bi_{0.33}/C was conducted respectively at -0.3 V in CO₂-saturated 0.1 M KHCO₃ for 12 h. In Fig. 3, Pd-Bi_{0.33}/C shows stably higher cathodic current density and FE(formate) compared to Pd/C. The FE(formate) maintains > 90% for 7 h, and slowly dwindle to ~75% after 12 h on Pd-Bi_{0.33}/C, while it drastically drops to ~20% after 12 h on Pd/C. The decreased FE(formate) and increased FE(H₂) may be correlated with surface CO accumulation (Fig. S9) and interfacial pH change [84–86]. Therefore, the higher durability of Pd-Bi_{0.33}/C during CO₂RRTF can be at least partly attributed to its higher CO_{ads} resistant property. The catalyst durability can also be testified by the constant current electrolysis at 4 mA cm⁻², as shown in Fig. S10.

3.2. CH mechanism for CO₂RRTF on Pd-based catalysts

The significantly higher activity, selectivity and durability for CO₂RRTF on Pd-Bi_{0.33}/C validates the hypothesis that FAD and CO₂RRTF can share an efficient Pd-based catalyst given that it features weakened adsorption of H* and *CO and strengthened adsorption of HCOO* compared to an intrinsic Pd catalyst. In fact, DFT calculations show that the d-band centers of Pd(111) and Pd(100) surfaces are down-shifted with Bi adatoms (the adsorption site of Bi adatoms is optimized in Fig. S11) as shown in Fig. 4a. The down-shifted d-band center is a descriptor for weakened adsorption of *CO and H* on Pd sites. Indeed, the CO adsorption energy on Pd(111) is lowered with Bi adatom modification (see Fig. S12), and the Gibbs free energies of H* at different sites of Pd(111) without and with Bi adatoms (Fig. 4b) show that Bi adatoms weaken H* adsorption as well, facilitating the reaction of H* with CO₂ to form formate according to the CH mechanism. Experimentally, the spectral feature of CO adsorption on the two catalysts in Fig. 4c shows that the band at ca. 1945 cm⁻¹ for bridge-bonded CO (CO_B) is significantly decreased relative to the linearly bonded CO (CO_L) band at ca. 2054 cm⁻¹, consistent with the weakened CO adsorption [20,78,87]. In contrast, the adsorption of HCOO* on Bi-modified Pd surfaces is otherwise enhanced, as will be discussed later. In short, the changed adsorption properties of relevant intermediates conform to the observed higher CO₂RRTF performance on Pd-Bi_{0.33}/C catalyst.

Potential dependent ATR-SEIRA spectra recorded on Pd/C and Pd-Bi_{0.33}/C in CO₂-saturated 0.1 M KHCO₃ are compared in Figs. 5a and 5b to identify the key intermediate in the CH mechanism for CO₂RRTF as well as to provide molecular level insights into the enhanced CO₂RRTF

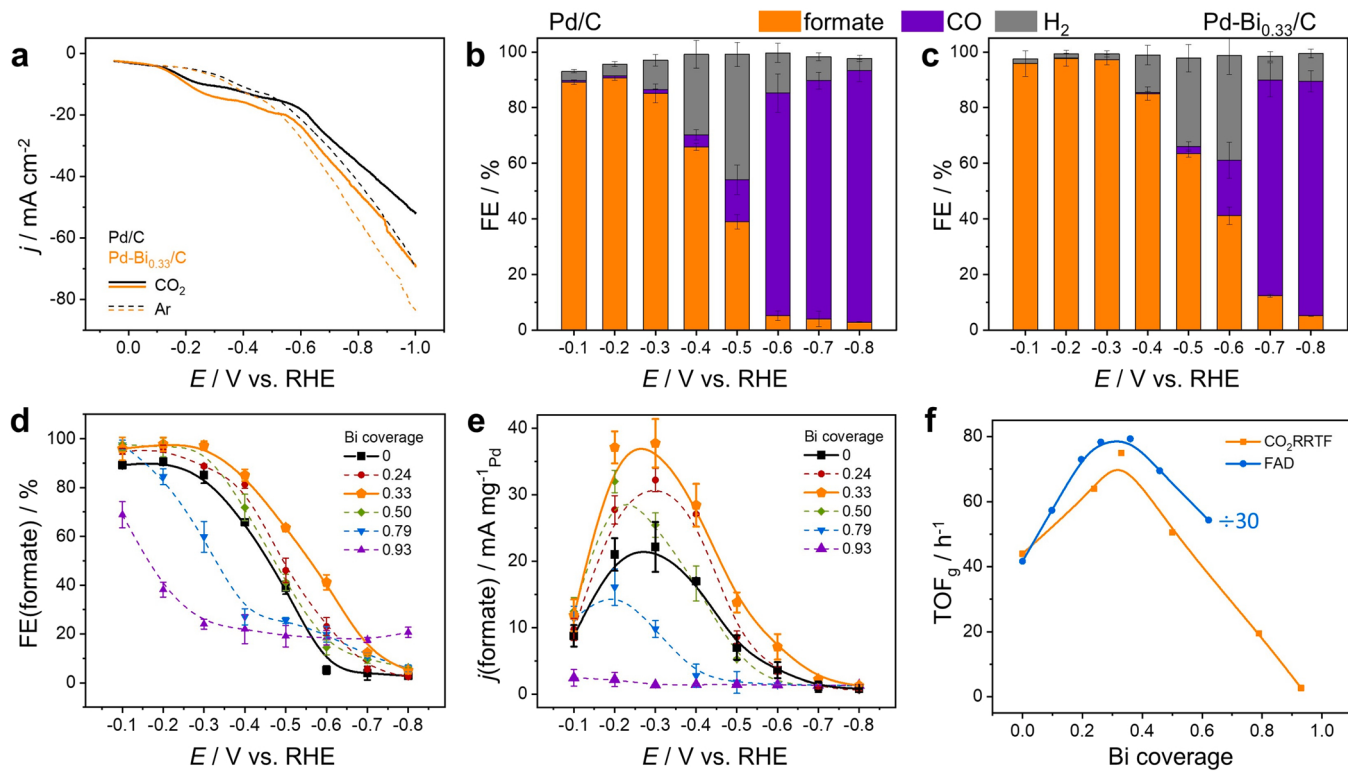


Fig. 2. (a) The LSVs of Pd/C and Pd-Bi_{0.33}/C in Ar- or CO₂-saturated 0.1 M KHCO₃ recorded at 50 mV s⁻¹. (b, c) The CO₂RR product distributions from -0.1 to -0.8 V for Pd/C and Pd-Bi_{0.33}/C. (d, e) Comparisons of FEs and partial currents for formate production on Pd/C and Pd-Bix/C. (f) Turnover frequencies based on global Pd sites (TOF_g) for CO₂RRTF on Pd-Bix/C at -0.3 V and FAD on Pd@Bi_{0.33}/C at 303 K as a function of Bi coverage. FAD data are adapted from Ref. 49.

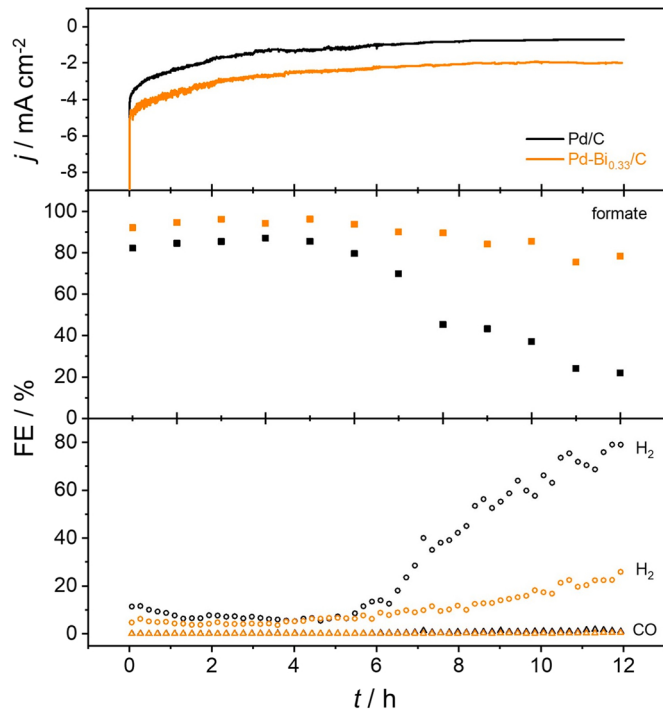


Fig. 3. Current densities (upper panel) and FEs (middle and lower panels) during chronoamperometric test on Pd/C and Pd-Bi_{0.33}/C at -0.3 V in CO₂-saturated 0.1 M KHCO₃ for 12 h.

performance with Bi adatoms. The peak assignments for these spectra are detailed in Table 1. Note that the relative CO coverages vary sigmoidally with negatively moving potential (see Figs. S13–S15), and

the Bi modification suppresses surface CO formation, consistent with the extended potential window for formate production on Pd-Bi_{0.33}/C. The potential at which CO_L peak arises coincides with the one where gaseous CO produces, in agreement to that CO_L is the final intermediate leading to gaseous CO [20].

Notably, a shoulder peak at 1680 cm⁻¹ (marked as asterisk in Figs. 5a and 5b), which is stronger on Pd-Bi_{0.33}/C than on Pd/C at potentials of formate production, deserves a close look. From peak fitting analysis as detailed in Fig. 5c and Fig. S16, the 1680 cm⁻¹ peak intensity exhibits a potential dependent volcano shape, maximizing at ca. -0.3 V, and the peak intensity is generally higher on Pd-Bi_{0.33}/C than on Pd/C (Fig. 5d), matching well with the potential dependent formate partial currents on these two catalysts. As a result, the 1680 cm⁻¹ peak is reasonably indexed to the C=O stretching vibration of the active formate intermediate. Using a single-beam spectrum at a neighboring potential as a reference spectrum helps to minimize the interference from the H₂O bending peak at 1620 cm⁻¹, enabling the ~1675 cm⁻¹ peak to be more clearly identified, as can be seen in Fig. S17.

Furthermore, the otherwise same experiment in deuterioxide was conducted to eliminate the partial overlap by the $\delta(\text{H}-\text{O}-\text{H})$ peak. As can be seen from Fig. 5e, the proposed $\nu(\text{C}=\text{O})$ peak for the intermediate red-shifts to ca. 1662 cm⁻¹ upon deuteration, consistent with the formate species for which H is directly bonded to ${}^*\text{C}=\text{O}$ and thus the $\nu(\text{C}=\text{O})$ frequency is affected, as can be roughly predicted by Eq. (1) [88].

$$\frac{\nu(\text{C}=\text{O}_{\text{OCDO}})}{\nu(\text{C}=\text{O}_{\text{OCHO}})} = \sqrt{\frac{m_{\text{CH}}m_{\text{O}}(m_{\text{CD}} + m_{\text{O}})}{m_{\text{CD}}m_{\text{O}}(m_{\text{CH}} + m_{\text{O}})}} = 0.98 \quad (1)$$

Along this line, the 1680 cm⁻¹ peak is unlikely due to multiply bonded CO (CO_M) or adsorbed carboxyl (*COOH), since H is either not present or not directly linked to C=O. In fact, the CO_M on Pd surfaces usually delivers a typical IR band higher than 1700 cm⁻¹ [20,21,24], while the *COOH delivers a band lower than 1600 cm⁻¹ [73,76,89,90].

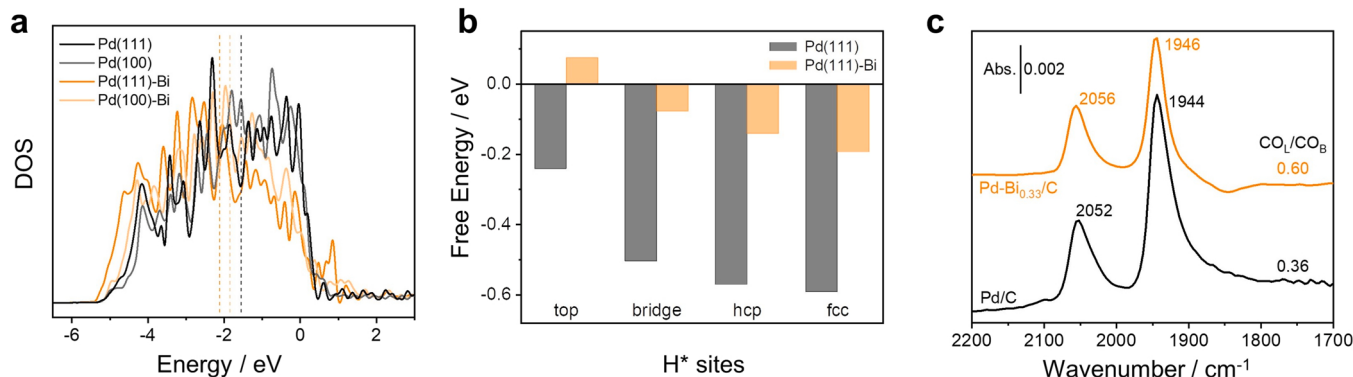


Fig. 4. (a) d-electron density of state of surface Pd atoms with or without Bi adatom decoration, the dotted line is the d-band center, and the energy of the horizontal axis is relative to the Fermi energy level. (b) The Gibbs free energies for H^* at different sites on Pd(111) and Pd(111)-Bi surfaces. (c) ATR-SEIRA spectra of CO adsorption on Pd/C and Pd-Bi_{0.33}/C at 0.5 V in CO-saturated 0.1 M KHCO₃.

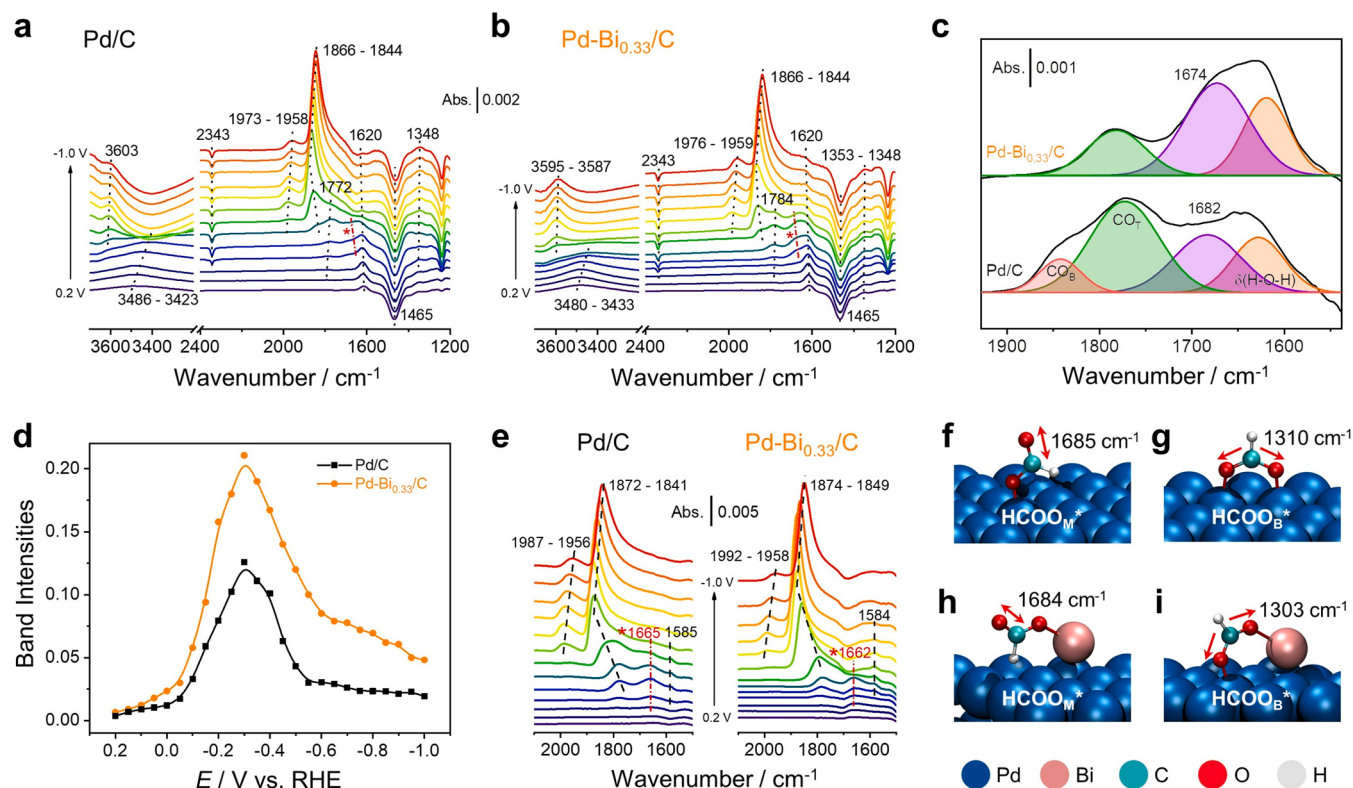


Fig. 5. (a, b) Potential-dependent ATR-SEIRA spectra for Pd/C and Pd-Bi_{0.33}/C in CO₂-saturated 0.1 M KHCO₃ from 0.2 to -1.0 V, with the spectrum taken at 0.4 V serving as the reference. The spectra are collected every 50 mV. (c) Deconvoluted ATR-SEIRA spectra acquired at -0.3 V in CO₂-saturated 0.1 M KHCO₃ on Pd/C and Pd-Bi_{0.33}/C. (d) Potential dependent HCOO* band intensities on Pd/C and Pd-Bi_{0.33}/C. (e) Potential-dependent ATR-SEIRA spectra for Pd/C and Pd-Bi_{0.33}/C in CO₂-saturated 0.1 M KDCO₃ in D₂O from 0.2 to -1.0 V, with the single-beam spectrum taken at 0.4 V serving as the reference. (f-i) Configurations and vibrational frequencies for formate adsorbed on Pd(111) and Pd(111)-Bi model surfaces.

The $\nu(C=O)$ frequencies for $^{*}COOH$ on Pd(111) with different H* coverages are also calculated in details (Table S4), all the results are discrepant from the observed 1680 cm⁻¹ peak.

The adsorption configuration of the formate intermediate is further clarified by DFT calculations. The frequencies of $\nu(C=O)$ for monodentate HCOO_M^{*} on Pd(111) (Fig. 5 f) and Pd(111)-Bi (Fig. 5 h) surfaces are 1678 and 1684 cm⁻¹, respectively, coinciding well with the observed peak position, while the symmetric stretch $\nu(OCO)$ band for the bidentate HCOO_B^{*} is located at 1310 and 1303 cm⁻¹ on Pd(111) (Fig. 5 g) and Pd(111)-Bi (Fig. 5 i) surfaces, respectively. The DFT calculations also indicate that the isotopic substitution of H by D in the HCOO_M^{*} species redshifts the $\nu(C=O)$ band by ca. 12 cm⁻¹, consistent

with the experimental result. Relevant vibrational frequencies were also calculated on H-covered Pd(111) surfaces, a Pd adatom on Pd(111) surface, and Pd(211)-Bi surface with three neighboring water layers, the results (Figs. S18-S20) are similar to those presented in Fig. 5f-i. The spectrometric and calculational results both suggest that HCOO_M^{*} with downward C-H bond is the last active intermediate leading to the formate product for the CO₂RR on Pd surfaces, and the Bi adatom modification favors the formation of the HCOO_M^{*}. In short, Pd is the main catalytic metal and Bi adatoms on Pd concertedly enhance the CO₂RR performance via electronic and geometric effects.

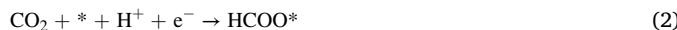
A kinetic analysis may help to distinguish the PCET and CH mechanisms for CO₂RR. In the PCET mechanism, the first step proton-

Table 1

The related peak assignments in Figs. 5a and 5b.

Peaks / cm^{-1}	Assignments
~3600	$\nu(\text{O-H})$ of co-adsorbed free H_2O
3200–3600	$\nu(\text{O-H})$ of interfacial H_2O with hydrogen bonding
2343	Dissolved CO_2
~1970	Linearly bonded CO_B
~1850	Bridge-bonded CO_B
~1780	Triply bonded CO_T
~1680	$\nu(\text{C=O})$ in HCOO_M^*
~1620	$\delta(\text{H-O-H})$ of interfacial H_2O
~1584	Dissolved HCOO^-
~1465	Adsorbed HCOO^- or CO_3^{2-} at positive potentials
~1350	Dissolved HCOO^-
1235	Si-O in Si prism

electron transfer is the rate determining step (RDS), as described by Eq. 2.



Thus, the Tafel slope for formate production should be 118 mV dec^{-1} assuming that the transfer coefficient (α) is 0.5. In the CH mechanism, the first step is the first electron transfer to form the H^* (Eq. 3), which is an energetic and kinetic favorable process on Pd surfaces (noting the underpotential deposited H is facilely formed on Pd at potentials 0.35–0.05 V, also see Supplementary Note 1 for more calculation details), and the hydrogenation step (Eq. 4) is the RDS.



At lower CO_2RR overpotentials (see below for an estimation of the equilibrium potential), Eq. (2) should be at an equilibrium state, which means that a single electron transfer takes place before the RDS, leading to a Tafel slope of 59 mV dec^{-1} . While at higher overpotentials, the backward reaction of Eq. 2 could be neglected. Based on the steady state approximation, the formation and consumption rate of H^* should be equal, leading to a Tafel slope of 118 mV dec^{-1} , see Supplementary Note 2 for the detailed derivation. Along this line, it is necessary to carefully analyze the Tafel slope for formate production at lower and higher overpotentials (both are limited to the formate production potential region). The linear scan voltammograms at 1 mV s^{-1} were recorded to obtain the formate partial currents at various potentials (Fig. 6a), given that the FE for formate approximately remained $> 90\%$ even at $+0.05 \text{ V}$ (see Fig. S21). Note that the standard reduction potential of $\text{CO}_2/\text{HCOO}^-$ is -0.02 V at pH 7. For such a very low HCOO^- concentration of $\sim 0.1 \text{ mM}$ after CO_2RR at $+0.05 \text{ V}$ for a sufficient time, the calculated equilibrium potential of the $\text{CO}_2/\text{HCOO}^-$ redox can be as high as ca. 0.10 V , validating the Tafel analysis over the potential range shown in Fig. 6b. Two linear segments of the Tafel plots yield the slopes at lower and higher overpotentials similar to those predicted by the CH

mechanism and consistent with the literature report [39]. Also noted in Fig. 6b, the apparent Tafel slope for formate production on $\text{Pd-Bi}_{0.33}/\text{C}$ is smaller than that on Pd/C , signifying a faster reduction kinetics on the former. To obtain a kinetically meaningful Tafel slope [91], a Tafel slope plot vs. potential is presented in Fig. 6c, basically showing two plateaus.

Although bidentate formate HCOO_B^* is widely assumed in the literature as the intermediate leading to the formate product in the solution, it should be noted that HCOO_B^* is favored at relatively positive potentials, as confirmed previously by potential dependent ATR-SEIRAS measurement of formic acid oxidation at Pd electrode [21]. It is often believed that HCOO_B^* binds to metal surfaces more strongly than HCOO_M^* . However, the relative adsorption strength of HCOO_B^* and HCOO_M^* may change with decreasing potential as in the case of CO_2RR . Actually, we calculate the relative adsorption Gibbs free energy for HCOO_M^* and HCOO_B^* with or without extra electrons introduced into the system. As shown in Fig. 7a, with extra electrons, i.e., at negative potentials, the binding strength of HCOO_M^* increases and may even surpasses that of HCOO_B^* . The DFT calculation results to some extent justify the energy aspect of the CH mechanism with HCOO_M^* as the immediate precursor for the formate product, which is consistent with the scaling relation between the coverage of HCOO_M^* and the formate production rate as shown in Fig. 5d.

The proposal that HCOO_M^* is the key intermediate for formate production in CO_2RR on the two Pd-based catalysts may find further support from the plots of Gibbs free energy as a function of the reaction coordinate according to the CH mechanism shown in Fig. 7b (see Table S5 for more details), with the geometric structures of the relevant intermediates shown in Fig. S22. A full H^* coverage is set to mimic the Pd surface when CO_2RR is overwhelming [26]. For the HCOOH pathway (the right reaction coordinate), Bi adatoms significantly stabilize the HCOO_M^* adsorption, with a much lower free energy span for the hydrogenation step, consistent with the higher selectivity and activity for formate on $\text{Pd-Bi}_{0.33}/\text{C}$. For the CO pathway (the left reaction coordinate), Bi-modification decreases the free energy span of ${}^*\text{COOH}$ and remarkably weakens the ${}^*\text{CO}$ adsorption, accounting for the suppressed CO pathway and the better CO tolerance of $\text{Pd-Bi}_{0.33}/\text{C}$.

4. Conclusions

In this work, we present an interactive study of catalyst and mechanism for CO_2RR on Pd surfaces that is effective in identifying a potent catalyst and updating the reaction pathway. On one hand, in light of existing reaction mechanisms of FAD and CO_2RR reactions, a hypothesis is put forward that an efficient catalyst can be shared for both FAD and CO_2RR . To demonstrate it, the $\text{Pd-Bi}_{0.33}/\text{C}$ ($\theta_{\text{Bi}} = 1/3$) once optimized for FAD has been selected as a prototype candidate catalyst for CO_2RR , and indeed exhibits the highest formate faradaic efficiency 97.7% at -0.2 V and the highest mass partial current $38.3 \text{ mA mg}_{\text{Pd}}^{-1}$ at -0.3 V among all the tested Pd-based catalysts, as well as a markedly higher durability. On the other hand, the reaction

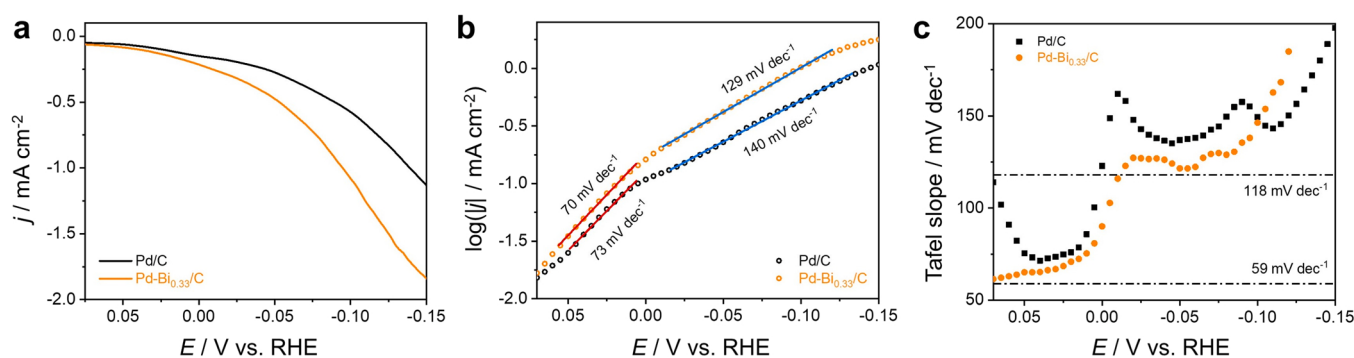


Fig. 6. (a) The LSVs for Pd/C and $\text{Pd-Bi}_{0.33}/\text{C}$ in CO_2 -saturated 0.1 M KHCO_3 recorded at 1 mV s^{-1} . (b) Tafel plot and (c) Tafel slope plot of the LSV scans.

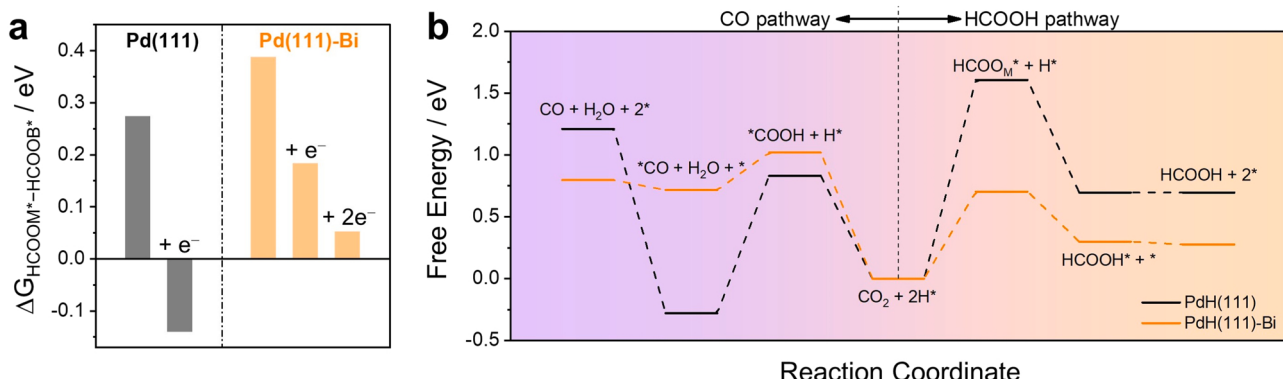


Fig. 7. (a) The relative adsorption Gibbs free energy for HCOOM^* and HCOOB^* with or without extra electrons introduced into the system. (b) Gibbs free energy diagrams for the HCOOH pathway and the CO pathway on $\text{PdH}(111)$ and $\text{PdH}(111)\text{-Bi}$ surfaces. All Gibbs free energies are shown relative to the initial state.

mechanism for CO_2RRTF at Pd surfaces is updated as a result of combined isotope labeled *in situ* ATR-SEIRAS measurement and DFT calculations. The key intermediate, i.e., HCOOM^* , of the CH mechanism for CO_2RRTF has been directly observed by *in situ* ATR-SEIRAS. Higher HCOOM^* coverage observed on $\text{Pd-Bi}_{0.33}/\text{C}$ conforms to its higher electrocatalytic performance for CO_2RRTF . DFT calculations also reveal that the HCOOM^* can be stabilized at negative potentials, and the HCOOH pathway is favored while the CO pathway is not on Bi-modified Pd surface, consistent with the experimental observation. The interactive study paradigm may be further extended to the mutual promotion of catalyst screening and mechanism understanding for more electrocatalytic reactions.

CRediT authorship contribution statement

Tian-Wen Jiang: Investigation, Methodology, Formal analysis, Visualization, Writing – original draft, Writing – review & editing. **Xianxian Qin:** Investigation, Formal analysis, Writing – review & editing. **Ke Ye:** Investigation, Methodology. **Wei-Yi Zhang:** Investigation, Methodology. **Hong Li:** Investigation, Methodology. **Wenhui Liu:** Investigation, Methodology. **Shengjuan Huo:** Investigation, Methodology. **Xia-Guang Zhang:** Investigation, Methodology, Formal analysis, Visualization, Writing – review & editing. **Kun Jiang:** Formal analysis, Visualization, Writing – review & editing. **Wen-Bin Cai:** Conceptualization, Formal analysis, Visualization, Supervision, Writing – review & editing.

Declaration of Competing Interest

The authors declare that they have no known competing financial interests or personal relationships that could have appeared to influence the work reported in this paper.

Data availability

Data will be made available on request.

Acknowledgements

This work was supported by the National Key R&D Program of China (2022YFA1503803 and 2022YFB4102000), the National Natural Science Foundation of China (21733004, 22002088 and 22002036), the Shanghai Science and Technology Innovation Action Plan (22dz1205500) and the Shanghai Sailing Program (20YF1420500).

Appendix A. Supporting information

Supplementary data associated with this article can be found in the

online version at doi:10.1016/j.apcatb.2023.122815.

References

- P. Sebastián-Pascual, S. Mezzavilla, I.E.L. Stephens, M. Escudero-Escribano, Structure-sensitivity and electrolyte effects in CO_2 electroreduction: from model studies to applications, *ChemCatChem* 11 (2019) 3626–3645.
- D.D. Zhu, J.L. Liu, S.Z. Qiao, Recent advances in inorganic heterogeneous electrocatalysts for reduction of carbon dioxide, *Adv. Mater.* 28 (2016) 3423–3452.
- M.G. Kibria, J.P. Edwards, C.M. Gabardo, C.T. Dinh, A. Seifitokaldani, D. Sinton, E.H. Sargent, Electrochemical CO_2 reduction into chemical feedstocks: from mechanistic electrocatalysis models to system design, *Adv. Mater.* 31 (2019), 1807166.
- M. Jouny, W. Luc, F. Jiao, General techno-economic analysis of CO_2 electrolysis systems, *Ind. Eng. Chem. Res.* 57 (2018) 2165–2177.
- P. De Luna, C. Hahn, D. Higgins, S.A. Jaffer, T.F. Jaramillo, E.H. Sargent, What would it take for renewably powered electrosynthesis to displace petrochemical processes? *Science* 364 (2019) eaav3506.
- J. Eppinger, K.-W. Huang, Formic acid as a hydrogen energy carrier, *ACS Energy Lett.* 2 (2016) 188–195.
- K. Sordakis, C.H. Tang, L.K. Vogt, H. Junge, P.J. Dyson, M. Beller, G. Laurenczy, Homogeneous catalysis for sustainable hydrogen storage in formic acid and alcohols, *Chem. Rev.* 118 (2018) 372–433.
- C.F. Shih, T. Zhang, J. Li, C. Bai, Powering the future with liquid sunshine, *Joule* 2 (2018) 1925–1949.
- S. Zhai, S. Jiang, C. Liu, Z. Li, T. Yu, L. Sun, G. Ren, W. Deng, Liquid sunshine: formic acid, *J. Phys. Chem. Lett.* 13 (2022) 8586–8600.
- Y. Hori, H. Wakebe, T. Tsukamoto, O. Koga, Electrocatalytic process of CO selectivity in electrochemical reduction of CO_2 at metal-electrodes in aqueous media, *Electrochim. Acta* 39 (1994) 1833–1839.
- S. Ikeda, T. Takagi, K. Ito, Selective formation of formic-acid, oxalic-acid, and carbon-monoxide by electrochemical reduction of carbon-dioxide, *Bull. Chem. Soc. Jpn.* 60 (1987) 2517–2522.
- H. Liu, J. Xia, N. Zhang, H. Cheng, W. Bi, X. Zu, W. Chu, H. Wu, C. Wu, Y. Xie, Solid-liquid phase transition induced electrocatalytic switching from hydrogen evolution to highly selective CO_2 reduction, *Nat. Catal.* 4 (2021) 202–211.
- N. Han, Y. Wang, H. Yang, J. Deng, J. Wu, Y. Li, Y. Li, Ultrathin bismuth nanosheets from *in situ* topotactic transformation for selective electrocatalytic CO_2 reduction to formate, *Nat. Commun.* 9 (2018) 1320.
- K. Fan, Y. Jia, Y. Ji, P. Kuang, B. Zhu, X. Liu, J. Yu, Curved surface boosts electrochemical CO_2 reduction to formate via bismuth nanotubes in a wide potential window, *ACS Catal.* 10 (2020) 358–364.
- C. Cao, D.D. Ma, J.F. Gu, X. Xie, G. Zeng, X. Li, S.G. Han, Q.L. Zhu, X.T. Wu, Q. Xu, Metal-organic layers leading to atomically thin bismuthene for efficient carbon dioxide electroreduction to liquid fuel, *Angew. Chem. Int. Ed.* 59 (2020) 15014–15020.
- I. Grigioni, L.K. Sagar, Y.C. Li, G. Lee, Y. Yan, K. Bertens, R.K. Miao, X. Wang, J. Abed, D.H. Won, F.P. García de Arquer, A.H. Ip, D. Sinton, E.H. Sargent, CO_2 electroreduction to formate at a partial current density of 930 mA cm^{-2} with in-p colloid quantum dot derived catalysts, *ACS Energy Lett.* 6 (2021) 79–84.
- J.Y. Li, M.H. Zhu, Y.F. Han, Recent advances in electrochemical CO_2 reduction on indium-based catalysts, *ChemCatChem* 13 (2021) 514–531.
- S. Zhang, B. Jiang, K. Jiang, W.B. Cai, Surfactant-free synthesis of carbon-supported palladium nanoparticles and size-dependent hydrogen production from formic acid-formate solution, *ACS Appl. Mater. Interfaces* 9 (2017) 24678–24687.
- X. Min, M.W. Kanan, Pd-catalyzed electrohydrogenation of carbon dioxide to formate: high mass activity at low overpotential and identification of the deactivation pathway, *J. Am. Chem. Soc.* 137 (2015) 4701–4708.
- T.W. Jiang, Y.W. Zhou, X.Y. Ma, X. Qin, H. Li, C. Ding, B. Jiang, K. Jiang, W.B. Cai, Spectrometric study of electrochemical CO_2 reduction on Pd and Pd-B electrodes, *ACS Catal.* 11 (2021) 840–848.

[21] J.Y. Wang, H.X. Zhang, K. Jiang, W.B. Cai, From HCOOH to CO at Pd electrodes: a surface-enhanced infrared spectroscopy study, *J. Am. Chem. Soc.* 133 (2011) 14876–14879.

[22] R. Kortlever, I. Peters, S. Koper, M.T.M. Koper, Electrochemical CO₂ reduction to formic acid at low overpotential and with high faradaic efficiency on carbon-supported bimetallic Pd–Pt nanoparticles, *ACS Catal.* 5 (2015) 3916–3923.

[23] K. Jiang, W.B. Cai, Carbon supported Pd–Pt–Cu nanocatalysts for formic acid electrooxidation: synthetic screening and componential functions, *Appl. Catal. B* 147 (2014) 185–192.

[24] H.X. Zhang, S.H. Wang, K. Jiang, T. André, W.B. Cai, In situ spectroscopic investigation of CO accumulation and poisoning on Pd black surfaces in concentrated HCOOH, *J. Power Sources* 199 (2012) 165–169.

[25] K. Jiang, K. Xu, S. Zou, W.B. Cai, B-doped Pd catalyst: boosting room-temperature hydrogen production from formic acid-formate solutions, *J. Am. Chem. Soc.* 136 (2014) 4861–4864.

[26] D. Gao, H. Zhou, F. Cai, D. Wang, Y. Hu, B. Jiang, W.B. Cai, X. Chen, R. Si, F. Yang, S. Miao, J. Wang, G. Wang, X. Bao, Switchable CO₂ electroreduction via engineering active phases of Pd nanoparticles, *Nano Res.* 10 (2017) 2181–2191.

[27] N. Han, M. Sun, Y. Zhou, J. Xu, C. Cheng, R. Zhou, L. Zhang, J. Luo, B. Huang, Y. Li, Alloyed palladium–silver nanowires enabling ultrastable carbon dioxide reduction to formate, *Adv. Mater.* 33 (2021), 2005821.

[28] J.S. Diercks, M. Georgi, J. Herranz, N. Diklic, P. Chauhan, A.H. Clark, R. Hubner, A. Faisnel, Q.H. Chen, M. Nachtegaal, A. Eychmüller, T.J. Schmidt, CO₂ electroreduction on unsupported PdPt aerogels: effects of alloying and surface composition on product selectivity, *ACS Appl. Energy Mater.* 5 (2022) 8460–8471.

[29] Y. Hou, R. Erni, R. Widmer, M. Rahaman, H. Guo, R. Fasel, P. Moreno-García, Y. Zhang, P. Broekmann, Synthesis and Characterization of Degradation-resistant Cu/CuPd nanowire catalysts for the efficient production of formate and CO from CO₂, *ChemElectroChem* 6 (2019) 3189–3198.

[30] H. Xie, Y. Wan, X. Wang, J. Liang, G. Lu, T. Wang, G. Chai, N.M. Adli, C. Priest, Y. Huang, G. Wu, Q. Li, Boosting Pd-catalysis for electrochemical CO₂ reduction to CO on Bi–Pd single atom alloy nanodendrites, *Appl. Catal. B* 289 (2021), 119783.

[31] X. Tan, C. Yu, X. Song, L. Ni, H. Xu, Y. Xie, Z. Wang, S. Cui, Y. Ren, W. Li, Y. Zhang, J. Qiu, Robust O–Pd–Cl catalyst–electrolyte interfaces enhance CO tolerance of Pd/C catalyst for stable CO₂ electroreduction, *Nano Energy* 104 (2022), 107957.

[32] H. Huang, H. Jia, Z. Liu, P. Gao, J. Zhao, Z. Luo, J. Yang, J. Zeng, Understanding of strain effects in the electrochemical reduction of CO₂ using Pd nanostructures as an ideal platform, *Angew. Chem. Int. Ed.* 56 (2017) 3594–3598.

[33] Y. Liang, J. Zhao, H. Zhang, A. Zhang, S. Wang, J. Li, M. Shakouri, Q. Xiao, Y. Hu, Z. Liu, Z. Geng, F. Li, J. Zeng, Bias-adaptable CO₂-to-CO conversion via tuning the binding of competing intermediates, *Nano Lett.* 21 (2021) 8924–8932.

[34] L. Jia, M. Sun, J. Xu, X. Zhao, R. Zhou, B. Pan, L. Wang, N. Han, B. Huang, Y. Li, Phase-dependent electrocatalytic CO₂ reduction on Pd3Bi Nanocrystals, *Angew. Chem. Int. Ed* 60 (2021) 21741–21745.

[35] L. Xie, X. Liu, F. Huang, J. Liang, J. Liu, T. Wang, L. Yang, R. Cao, Q. Li, Regulating Pd-catalysis for electrocatalytic CO₂ reduction to formate via intermetallic PdBi nanosheets, *Chin. J. Catal.* 43 (2022) 1680–1686.

[36] Y. Zhou, R. Zhou, X. Zhu, N. Han, B. Song, T. Liu, G. Hu, Y. Li, J. Lu, Y. Li, Mesoporous PdAg nanospheres for stable electrochemical CO₂ reduction to formate, *Adv. Mater.* 32 (2020), 2000992.

[37] H. Lv, F. Lv, H. Qin, X. Min, L. Sun, N. Han, D. Xu, Y. Li, B. Liu, Single-crystalline mesoporous palladium and palladium-copper nanocubes for highly efficient electrochemical CO₂ reduction, *CCS Chem.* 4 (2022) 1376–1385.

[38] S. Guo, Y. Liu, E. Murphy, A. Ly, M. Xu, I. Matanovic, X. Pan, P. Atanassov, Robust palladium hydride catalyst for electrocatalytic formate formation with high CO tolerance, *Appl. Catal. B* 316 (2022), 121659.

[39] M.J.W. Blom, W.P.M. van Swaaij, G. Mul, S.R.A. Kersten, Mechanism and micro kinetic model for electroreduction of CO₂ on Pd/C: the role of different palladium hydride phases, *ACS Catal.* 11 (2021) 6883–6891.

[40] B. Jiang, X.G. Zhang, K. Jiang, D.Y. Wu, W.B. Cai, Boosting formate production in electrocatalytic CO₂ reduction over wide potential window on Pd surfaces, *J. Am. Chem. Soc.* 140 (2018) 2880–2889.

[41] M.T.M. Koper, Thermodynamic theory of multi-electron transfer reactions: implications for electrocatalysis, *J. Electroanal. Chem.* 660 (2011) 254–260.

[42] G.C. Luque, M.R.G. de Chialvo, A.C. Chialvo, Influence of spontaneous decomposition on the electrochemical formic acid oxidation on a nanostructured palladium electrode, *Electrochem. Commun.* 70 (2016) 69–72.

[43] J.S. Diercks, J. Herranz, M. Georgi, N. Diklić, P. Chauhan, K. Ebner, A.H. Clark, M. Nachtegaal, A. Eychmüller, T.J. Schmidt, Interplay between surface-adsorbed CO and bulk Pd hydride under CO₂-electroreduction conditions, *ACS Catal.* 12 (2022) 10727–10741.

[44] S. Pérez-Rodríguez, N. Rillo, M.J. Lázaro, E. Pastor, Pd catalysts supported onto nanostructured carbon materials for CO₂ valorization by electrochemical reduction, *Appl. Catal. B* 163 (2015) 83–95.

[45] W.J. Durand, A.A. Peterson, F. Studt, F. Abild-Pedersen, J.K. Nørskov, Structure effects on the energetics of the electrochemical reduction of CO₂ by copper surfaces, *Surf. Sci.* 605 (2011) 1354–1359.

[46] P. Wang, S.N. Steinmann, G. Fu, C. Michel, P. Sautet, Key role of anionic doping for H₂ production from formic acid on Pd(111), *ACS Catal.* 7 (2017) 1955–1959.

[47] J.S. Yoo, F. Abild-Pedersen, J.K. Nørskov, F. Studt, Theoretical analysis of transition-metal catalysts for formic acid decomposition, *ACS Catal.* 4 (2014) 1226–1233.

[48] R. Kortlever, J. Shen, K.J.P. Schouten, F. Calle-Vallejo, M.T.M. Koper, Catalysts and reaction pathways for the electrochemical reduction of carbon dioxide, *J. Phys. Chem. Lett.* 6 (2015) 4073–4082.

[49] J.T. Feaster, C. Shi, E.R. Cave, T. Hatsukade, D.N. Abram, K.P. Kuhl, C. Hahn, J. K. Nørskov, T.F. Jaramillo, Understanding selectivity for the electrochemical reduction of carbon dioxide to formic acid and carbon monoxide on metal electrodes, *ACS Catal.* 7 (2017) 4822–4827.

[50] K. Mori, H. Hata, H. Yamashita, Interplay of Pd ensemble sites induced by GaO modification in boosting CO₂ hydrogenation to formic acid, *Appl. Catal. B* 320 (2023), 122022.

[51] X. Qin, H. Li, S. Xie, K. Li, T.W. Jiang, X.Y. Ma, K. Jiang, Q. Zhang, O. Terasaki, Z. Wu, W.B. Cai, Mechanistic analysis-guided Pd-based catalysts for efficient hydrogen production from formic acid dehydrogenation, *ACS Catal.* 10 (2020) 3921–3932.

[52] S.Y. Wu, H.T. Chen, CO₂ electrochemical reduction catalyzed by graphene supported palladium cluster: a computational guideline, *ACS Appl. Energy Mater.* 2 (2019) 1544–1552.

[53] S. Zhang, P. Kang, T.J. Meyer, Nanostructured tin catalysts for selective electrochemical reduction of carbon dioxide to formate, *J. Am. Chem. Soc.* 136 (2014) 1734–1737.

[54] A. Bagger, W. Ju, A.S. Varela, P. Strasser, J. Rossmeisl, Electrochemical CO₂ reduction: a classification problem, *ChemPhysChem* 18 (2017) 3266–3273.

[55] C.H. Lee, M.W. Kanan, Controlling H⁺ vs CO₂ reduction selectivity on Pb electrodes, *ACS Catal.* 5 (2015) 465–469.

[56] Y. Qiao, W.C. Lai, K. Huang, T.T. Yu, Q.Y. Wang, L. Gao, Z.L. Yang, Z.S. Ma, T. L. Sun, M. Liu, C. Lian, H.W. Huang, Engineering the local microenvironment over Bi nanosheets for highly selective electrocatalytic conversion of CO₂ to HCOOH in strong acid, *ACS Catal.* 12 (2022) 2357–2364.

[57] H. Xie, T. Zhang, R. Xie, Z. Hou, X. Ji, Y. Pang, S. Chen, M.M. Titirici, H. Weng, G. Chai, Facet engineering to regulate surface states of topological crystalline insulator bismuth rhombic dodecahedrons for highly energy efficient electrochemical CO₂ reduction, *Adv. Mater.* 33 (2021), 2008373.

[58] W. Sheng, S. Kattel, S. Yao, B. Yan, Z. Liang, C.J. Hawkhurst, Q. Wu, J.G. Chen, Electrochemical reduction of CO₂ to synthesis gas with controlled CO/H₂ ratios, *Energy Environ. Sci.* 10 (2017) 1180–1185.

[59] W. Zhu, S. Kattel, F. Jiao, J.G. Chen, Shape-controlled CO₂ electrochemical reduction on nanosized Pd hydride cubes and octahedra, *Adv. Energy Mater.* 9 (2019), 1802840.

[60] C.J. Stalder, S. Chao, M.S. Wrighton, Electrochemical reduction of aqueous bicarbonate to formate with high-current efficiency near the thermodynamic potential at chemically derivatized electrodes, *J. Am. Chem. Soc.* 106 (1984) 3673–3675.

[61] H. Yoshitake, K. Takahashi, K. Ota, Electrochemical reduction of CO₂ on hydrogen-enriched and hydrogen-depleted surfaces, *J. Chem. Soc. Faraday Trans.* 90 (1994) 155–159.

[62] B.I. Podlovchenko, E.A. Kolyadko, S.G. Lu, Electroreduction of carbon-dioxide on palladium electrodes at potentials higher than the reversible hydrogen potential, *J. Electroanal. Chem.* 373 (1994) 185–187.

[63] C. Iwakura, S. Takezawa, H. Inoue, Catalytic reduction of carbon dioxide with atomic hydrogen permeating through palladized Pd sheet electrodes, *J. Electroanal. Chem.* 459 (1998) 167–169.

[64] F. Cai, D. Gao, H. Zhou, G. Wang, T. He, H. Gong, S. Miao, F. Yang, J. Wang, X. Bao, Electrochemical promotion of catalysis over Pd nanoparticles for CO₂ reduction, *Chem. Sci.* 8 (2017) 2569–2573.

[65] T. Cheng, H. Xiao, W.A. Goddard, Reaction mechanisms for the electrochemical reduction of CO₂ to CO and formate on the Cu(100) surface at 298 K from quantum mechanics free energy calculations with explicit water, *J. Am. Chem. Soc.* 138 (2016) 13802–13805.

[66] J. Quan, F. Muttaqien, T. Kondo, T. Kozarashi, T. Mogi, T. Imabayashi, Y. Hamamoto, K. Imagaki, I. Hamada, Y. Morikawa, J. Nakamura, Vibration-driven reaction of CO₂ on Cu surfaces via Eley-Rideal-type Mechanism, *Nat. Chem.* 11 (2019) 722–729.

[67] M.T. Tang, H. Peng, P.S. Lamoureux, M. Bajdich, F. Abild-Pedersen, From electricity to fuels: descriptors for c1 selectivity in electrochemical CO₂ reduction, *Appl. Catal. B* 279 (2020), 119384.

[68] J. Ryu, S. Surendranath, Polarization-induced Local pH swing promotes Pd-catalyzed CO₂ hydrogenation, *J. Am. Chem. Soc.* 142 (2020) 13384–13390.

[69] B. Peng, H.F. Wang, Z.P. Liu, W.B. Cai, Combined surface-enhanced infrared spectroscopy and first-principles study on electro-oxidation of formic acid at Sb-modified Pt electrodes, *J. Phys. Chem. C* 114 (2010) 3102–3107.

[70] Y.X. Chen, M. Heinen, Z. Jusys, R.J. Behm, Kinetics and mechanism of the electrooxidation of formic acid - spectroelectrochemical studies in a flow cell, *Angew. Chem. Int. Ed.* 45 (2006) 981–985.

[71] G. Samjeske, A. Miki, S. Ye, M. Osawa, Mechanistic study of electrocatalytic oxidation of formic acid at platinum in acidic solution by time-resolved surface-enhanced infrared absorption spectroscopy, *J. Phys. Chem. B* 110 (2006) 16559–16566.

[72] Y.W. Zhou, Y.F. Chen, K. Jiang, Z. Liu, Z.J. Mao, W.Y. Zhang, W.F. Lin, W.B. Cai, Probing the enhanced methanol electrooxidation mechanism on platinum-metal oxide catalyst, *Appl. Catal. B* 280 (2021), 119393.

[73] S. Zhu, B. Jiang, W.B. Cai, M. Shao, Direct observation on reaction intermediates and the role of bicarbonate anions in CO₂ electrochemical reduction reaction on Cu surfaces, *J. Am. Chem. Soc.* 139 (2017) 15664–15667.

[74] M. Moradzaman, G. Mul, Infrared analysis of interfacial phenomena during electrochemical reduction of CO₂ over polycrystalline copper electrodes, *ACS Catal.* 10 (2020) 8049–8057.

[75] J. Heyes, M. Dunwell, B.J. Xu, CO₂ reduction on Cu at low overpotentials with surface-enhanced in situ spectroscopy, *J. Phys. Chem. C* 120 (2016) 17334–17341.

[76] Y. Katayama, F. Nattino, L. Giordano, J. Hwang, R.R. Rao, O. Andreussi, N. Marzari, Y. Shao-Horn, An in situ surface-enhanced infrared absorption spectroscopy study of electrochemical CO_2 reduction: selectivity dependence on surface C-bound and O-bound reaction intermediates, *J. Phys. Chem. C* 123 (2019) 5951–5963.

[77] D. Gao, H. Zhou, J. Wang, S. Miao, F. Yang, G. Wang, J. Wang, X. Bao, Size-dependent electrocatalytic reduction of CO_2 over Pd nanoparticles, *J. Am. Chem. Soc.* 137 (2015) 4288–4291.

[78] Y.G. Yan, Q.X. Li, S.J. Huo, M. Ma, W.B. Cai, M. Osawa, Ubiquitous strategy for probing ATR surface-enhanced infrared absorption at platinum group metal-electrolyte interfaces, *J. Phys. Chem. B* 109 (2005) 7900–7906.

[79] G. Kresse, J. Furthmüller, Efficient iterative schemes for ab initio total-energy calculations using a plane-wave basis set, *Phys. Rev. B* 54 (1996) 11169–11186.

[80] K. Mathew, R. Sundararaman, K. Letchworth-Weaver, T.A. Arias, R.G. Hennig, Implicit solvation model for density-functional study of nanocrystal surfaces and reaction pathways, *J. Chem. Phys.* 140 (2014), 084106.

[81] K. Mathew, V.S.C. Kolluru, S. Mula, S.N. Steinmann, R.G. Hennig, Implicit self-consistent electrolyte model in plane-wave density-functional theory, *J. Chem. Phys.* 151 (2019), 234101.

[82] H. Wang, B. Jiang, T.T. Zhao, K. Jiang, Y.Y. Yang, J. Zhang, Z. Xie, W.B. Cai, Electrocatalysis of ethylene glycol oxidation on bare and Bi-modified Pd concave nanocubes in alkaline solution: an interfacial infrared spectroscopic investigation, *ACS Catal.* 7 (2017) 2033–2041.

[83] M. Wang, X. Qin, K. Jiang, Y. Dong, M. Shao, W.B. Cai, Electrocatalytic activities of oxygen reduction reaction on Pd/C and Pd–B/C catalysts, *J. Phys. Chem. C* 121 (2017) 3416–3423.

[84] M.R. Singh, Y. Kwon, Y. Lum, J.W. Ager III, A.T. Bell, Hydrolysis of electrolyte cations enhances the electrochemical reduction of CO_2 over Ag and Cu, *J. Am. Chem. Soc.* 138 (2016) 13006–13012.

[85] A.S. Varela, M. Kroschel, T. Reier, P. Strasser, Controlling the selectivity of CO_2 electroreduction on copper: the effect of the electrolyte concentration and the importance of the local pH, *Catal. Today* 260 (2016) 8–13.

[86] N. Gupta, M. Gattrell, B. MacDougall, Calculation for the cathode surface concentrations in the electrochemical reduction of CO_2 in KHCO_3 solutions, *J. Appl. Electrochem* 36 (2006) 161–172.

[87] P. Gelin, A.R. Siedle, J.T. Yates, Stoichiometric adsorbate species interconversion processes in the chemisorbed layer. An infrared study of the Co/Pd system, *J. Phys. Chem.* 88 (1984) 2978–2985.

[88] J.C. Dong, X.G. Zhang, V. Briega-Martos, X. Jin, J. Yang, S. Chen, Z.L. Yang, D. Y. Wu, J.M. Feliu, C.T. Williams, Z.Q. Tian, J.F. Li, In situ Raman spectroscopic evidence for oxygen reduction reaction intermediates at platinum single-crystal surfaces, *Nat. Energy* 4 (2019) 60–67.

[89] Y. Katayama, L. Giordano, R.R. Rao, J. Hwang, H. Muroyama, T. Matsui, K. Eguchi, Y. Shao-Horn, Surface (electro)chemistry of CO_2 on Pt surface: an in situ surface-enhanced infrared absorption spectroscopy study, *J. Phys. Chem. C* 122 (2018) 12341–12349.

[90] J.E. Pander, M.F. Baruch, A.B. Bocarsly, Probing the mechanism of aqueous CO_2 reduction on post-transition-metal electrodes using ATR-IR spectroelectrochemistry, *ACS Catal.* 6 (2016) 7824–7833.

[91] O. van der Heijden, S. Park, J.J.J. Eggebeen, M.T.M. Koper, Non-kinetic effects convolute activity and tafel analysis for the alkaline oxygen evolution reaction on NiFeOOH electrocatalysts, *Angew. Chem. Int. Ed.* 135 (2023), e202216477.